Vis Geosci
DOI 10.1007/s10069-007-0007-2

ORIGINAL ARTICLE

AUTHOR PROOF

Visualization of time-dependent dynamics of postglacial rebound

Ladislav Hanyk · David A. Yuen · Ctirad Matyska · Jakub Velímský

Received: 13 December 2006 / Revised: 21 May 2007 / Accepted: 23 May 2007

Abstract Postglacial rebound is a major geological process which plays an important role in many areas in the earth sciences. Up to now, most of the images derived from studies of the glacial isostatic adjustment phenomenon have been concerned with surface signatures, such as the uplift and gravity anomalies and not much attention has been paid on the dynamical responses in the mantle. We will make use of the 3D visualization package Amira to depict both the external and internal deformation histories of the transient viscoelastic flow inside the mantle induced by postglacial uplift. Of particularly great interest are the transient displacement fields and shear heating inside the mantle. This same visualization technology can be brought to bear in the future for visualizing tsunami waves in ocean basins excited by earthquakes, volcanic eruptions and InSAR images. We have also integrated the visualization results into the Google Earth virtual globe by combining this scheme with the Amira package to provide a better geographical and dynamical context.

Keywords Amira package · Google earth · Postglacial rebound · Piscoelastic flow · 3D visualization

Introduction

In the past, 2 million years ice ages have imposed periodically on the Earth's surface an extensive load of ice with a thickness of several kilometres and spanning horizontally three to four thousand kilometres (Hays et al. 1976; Peltier 1994; Siegert 2001). This substantial load, which we have visualized with the Amira package (Fig. 1) and the Google Earth virtual globe (Movie 1; all referenced movies can be found at http://www.geo.mff.cuni.cz/~lh/papers/07visgeo, http://www.msi.umn.edu/~ladah/07visgeo), caused a transient viscous flow with a global character to occur in the Earth's mantle. The subsequent dynamical reaction of the Earth's crust to this underlying mantle circulation is called postglacial rebound (e.g., Cathles 1975; Wu et al. 1998; Tromp and Mitrovica 2000; Mitrovica and Vermeersen 2002; Latychev et al. 2005), which has been employed by geophysicists to investigate many geophysical facets of the mantle, such as its viscosity structure and recent episodes of ice-melting associated with global warming (Velicogna and Wahr 2002).

Over the past 30 years, postglacial rebound has been a subject of intense interest in the geosciences, because it impacts numerous disciplines ranging from mantle viscosity (Peltier 1974; Mitrovica and Forte 2004) to postseismic deformation (Hetland and Hager 2006) and climate dynamics (Alley et al. 2005). Yet the visualization of the time-dependent dynamics of postglacial rebound has not been keeping pace with the advances in visualization made in other areas of geodynamics, such as mantle convection and earthquake dynamics. Erlebacher et al. (2001) gave a review of the current status of visualization in the geosciences and this poignant issue has also been discussed in the report on high-performance computing in the geosciences by Cohen (2005).

Electronic supplementary material The online version of this article (doi:10.1007/s10069-007-0007-2) contains supplementary material, which is available to authorized users.

L. Hanyk (✉) · C. Matyska · J. Velímský
Faculty of Mathematics and Physics, Department of Geophysics, Charles University, 18000 Prague, Czech Republic
e-mail: ladislav.hanyk@mff.cuni.cz

D. A. Yuen
Department of Geology and Geophysics and Minnesota Supercomputing Institute, University of Minnesota, Minneapolis, MN 55455, USA

Journal : 10069 | Dispatch : 26-6-2007 | Pages : 11
Article No. : 7 | ☐ LE | ☐ TYPESET
MS Code : 7 | ☑ CP | ☑ DISK

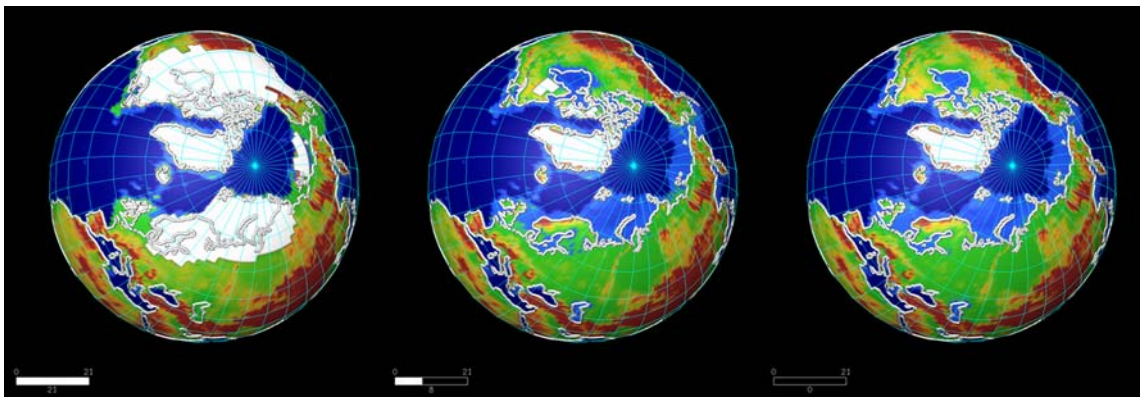

Fig. 1 Topographic heights and the ice-sheets retreat by ICE-4G (Peltier 1994) on the northern hemisphere from 21 (*left panel*) and 8 kyr (*middle panel*) before present until today (*right panel*). Both uplifting areas (Hudson Bay) and spreading of the oceans (Bering Bridge, North Sea) can be observed. All 22 time levels of the ICE-4G model are displayed in Movie 1 visualized by Amira images overlaying the northern hemisphere of Google Earth

With the exception of the works by Spada et al. (1992) and Hanyk et al. (2005) on time-dependent stress fields induced in the mantle by ice loading, all of the visualization of postglacial rebound has been focused on surface signatures such as uplift (Peltier 1974) and gravity signals (Wu and Peltier 1982). The images displayed have been rendered with standard 2D packages, such as Tecplot or GMT. Our past efforts in this area has mostly been concentrated on relaxation diagrams of the decay times associated with free-decaying modes (e. g., Sabadini and Vermeersen 2004) and its distinct comparison with the initial-value approaches of the surface responses (Hanyk et al. 1996, 1998). It was not until a few years ago (Hanyk et al. 2002) that we started to take advantage of the recent advances in visualization software such as Amira, described previously in Erlebacher et al. (2001), in the postglacial rebound problem. Some of these results can be found in Hanyk et al. (2005), where they showed the temporal evolution of the viscous heating distribution produced by the transient mantle flow. The phenomenon of viscous heating caused by tidal forcing was discussed by Prockter et al. (2005). In this technically oriented paper, we will elaborate in greater details the entire procedure, which went into this visualization effort, in order for others to learn about the necessary know-how in utilizing this state-of-the-art system, which can also be implemented in the framework of a web service (Erlebacher et al. 2006).

In "Ice models and methods for numerical solutions and visualization" we present the basic elements of our modelling and visualization procedures. Next, we give in "Visualization results" some characteristic examples of postglacial rebound dynamics, where seven movies will accompany the text and figures. Finally, we summarize our findings and give some perspectives for the future, such as applications in other geophysical endeavours. We will also discuss about the combination of Google Earth software with the Amira visualization package.

Ice models and methods for numerical solutions and visualization

The geographical load of ice and its time history represent the essential ingredients of the rebound problem. The paleotopographic models ICE-4G (Peltier 1994) and ICE-5G (Peltier 2004) of the ice sheets disintegration provide series of time-evolving datasets with topographic heights and an ice-coverage function on the spherical grids, which cover the period lasting from the last glacial maximum 21,000 years ago until the present time. In the three panels of Fig. 1, we show the ice coverage today and at 8 and 21 kyr before present, while Movie 1 (http://www.geo.mff.cuni.cz/~lh/papers/07visgeo, http://www.msi.umn.edu/~ladah/07visgeo) displays the retreating ice sheets over North America in all the 22 time levels. The images are prepared in the Amira package, Movie 1 has been constructed from using both Amira and Google Earth. Additional technical details concerning the implementation are provided in "Appendix A".

We employ spherical Earth models with compressible viscoelasticity. The models are all characterized by radial profiles of physical parameters (see also Hanyk et al. 2002). The viscoelastic rheology we have chosen is called a Maxwell body (Ranalli 1995), where for a short time it behaves elastically, while for longer duration, greater than several hundred years in the mantle, it behaves like a viscous fluid. The density ρ, implied gravitational acceleration g, the shear modulus μ and the bulk modulus K are adopted from the PREM model (Dziewonski and Anderson 1981) and we show them in Fig. 2. As in most of the postglacial rebound models, we will employ a one-dimensional, radially

Journal : 10069 Dispatch : 26-6-2007 Pages : 11
Article No. : 7 ☐ LE ☐ TYPESET
MS Code : 7 ☑ CP ☑ DISK

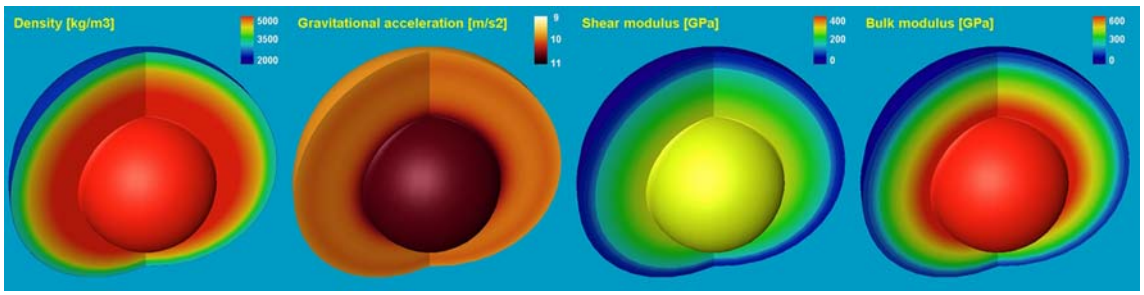

Fig. 2 Colored profiles of density, gravitational acceleration, shear and bulk modulus (from left to right) in the mantle as defined by the radially dependent model PREM (Dziewonski and Anderson 1981). The maximum values of all these physical parameters are reached at the bottom of the mantle, i.e., in the depth of 2,891 km: 5,566 kg/m^3, 10.68 m/s^2, 294 and 656 GPa

dependent viscosity profile. Models of mantle viscosity η that we selected are shown in Fig. 3: an isoviscous model M1 with the value of 10^{21} Pa s, a continuous viscosity profile M2 with a maximum of 1.6×10^{23} Pa s at the depth of 2,100 km and 10^{21} Pa s in the upper mantle, a model M3 similar to M2 but with a zone of low viscosity (10^{19} Pa s) between the depths of 110 and 220 km and a model M4 similar as M3 with a 270-km thick transition zone of 2×10^{22} Pa s at the bottom of the upper mantle (Hanyk et al. 1998).

The ice-loading model is an important input function in the postglacial rebound problem. A simplified ice sheet model we use here is a circular disc with a constant radius of over 1,600 km (15) and parabolic cross-sections as depicted in Fig. 4. More sophisticated types of ice sheet modelling can be found in Mitrovica and Vermeersen (2002). We have modelled the time history of ice ages with a simple time dependence, which captures the basic features of ice loading and disappearing. The ice age cycle lasting 100 kyr is simulated by a linearly increasing height of the whole disc during the first 90 kyr, followed by a disintegration period of 10 kyr with a linearly decreasing height. To demonstrate the relaxation properties of the viscoelastic Earth, we append to this one ice cycle additional 50 kyr without any surface loading.

The mathematical formulation of the differential equations governing the postglacial rebound process is described in Hanyk et al. (2002). The layout of the numerical implementation based on the method of lines (Schiesser 1994) and the input and output data are summarized in a flowchart shown in Fig. 5.

We have prepared most of the figures in the Amira visualization package. We mimic our time-dependent 3D data fields by a time series of images which consist of 2D hollow spherical shells with interior surfaces. While this configuration allows for a satisfactory 3D sensation of both surficial and internal dynamics, the need of large enough computer memory is considerably reduced, which gives the user the ability to handle interactively very long time series of these datasets. The time evolution of the growing and retreating ice sheet +model is imitated by the line-segment data format. A description of the process of visualizing the

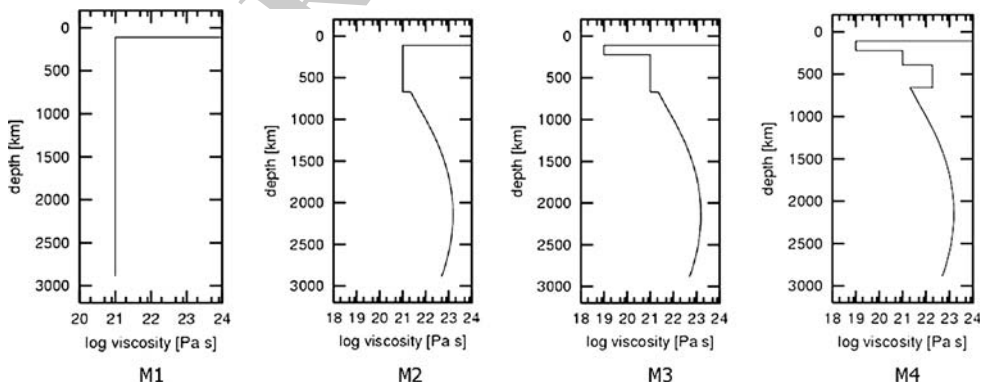

Fig. 3 Four radially-dependent profiles of mantle viscosity from the depth of 110 km down to the core-mantle boundary at 2,891 km: isoviscous M1 (10^{21} Pa s), M2 with the isoviscous upper mantle and continuously varying lower-mantle viscosity with a maximum of 1.6×10^{23} Pa s, M3 with the M2-like lower mantle and a low-viscosity zone between the depths of 110 and 220 km, and M4, which is M3 with a transition layer of 2×10^{22} Pa s in the depth of 400–670 km. The top 110 km of all our viscoelastic Earth models are considered to be elastic, i.e., with infinite viscosity

Journal : 10069 Dispatch : 26-6-2007 Pages : 11
Article No. : 7 LE TYPESET
MS Code : 7 CP DISK

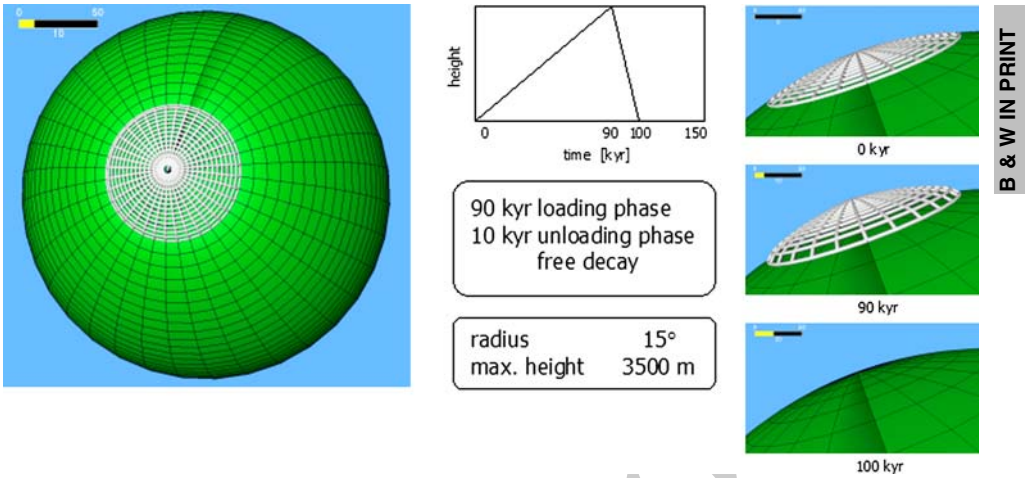

Fig. 4 Axisymmetric ice-sheet model with parabolic cross-sections, a constant radius and heights varying in time. The ice-age cycle is simplified by three subsequent phases: the disc height increases to the maximum during the first 90 kyr, then it rapidly decreases to zero and the Earth models are then allowed to relax viscoelastically with no surface loading

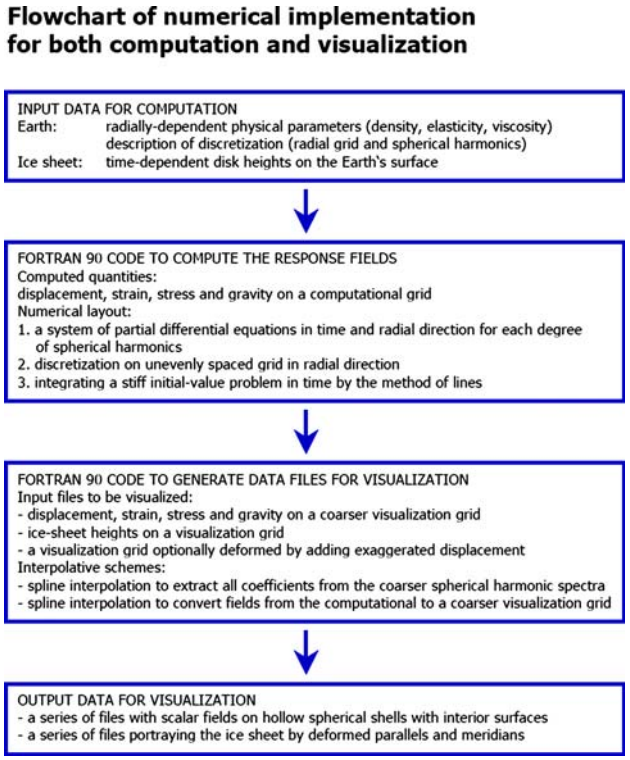

Fig. 5 Flowchart of the numerical implementation for both computation and visualization

output data along with some technically related comments is collected in "Appendix B".

Visualization results

We are foremost concerned with visualizing the rebound dynamics of the viscoelastic Earth models, caused by the surface loading, by means of monitoring the components of the displacement vector. We mark the panels with the vertical and horizontal displacement by U and V, respectively. The depression in the vertical direction is expressed by the red color and the blue colur denotes the uplift, while the red in the horizontal direction points out the movement off the axis and the blue again the opposite.

The simple spherical model constructed from three layers—a liquid core, a viscoelastic mantle and an elastic lithosphere—is considered in Fig. 6. The most important physical parameter for the response of this simple model is the bulk modulus K. We mark the panels with the incompressible model (with the infinite value of K) by I and those with the compressible model by C. Spherical shells as discussed in Appendix B are employed to visualize the radial and tangential displacement components U and V at 90 and 110 kyr (load maximum and 10 kyr after the ice melting, respectively) in Fig. 6 and from 0 to 1000 kyr in Movie 2 (http://www.geo.mff.cuni.cz/~lh/papers/07visgeo, http://www.msi.umn.edu/~ladah/07visgeo). While in the incompressible model the displacement converges to zero with relaxation times of the order of 10^4 yr, a gravitational instability emerges with the rise time of the same order in the compressible model (Plag and Jüttner 1995; Hanyk et al. 1999). We do not see the physical manifestation of the gravitational collapse but rather an indication that the linearised differential equations fail for the simple compressible model over the time scale of the rise time.

Next, we present the corresponding results for the PREM model and the viscosity profile M2 with high viscosity in the lower mantle. The realistic Earth model is loaded by the 100-kyr lasting ice cycle and let to relax viscoelastically. As we can observe in Fig. 7 and Movie 3, both the incompressible and compressible models are stable during the whole period. We can visually inspect which parts of the Earth are influenced by the surface load of the 15 radius. By comparing the left and right columns (best visible at 90 kyr) we observe that the depression below the ice sheet in the compressible model reaches the magnitude

Journal : 10069 Dispatch : 26-6-2007 Pages : 11
Article No. : 7 LE TYPESET
MS Code : 7 CP DISK

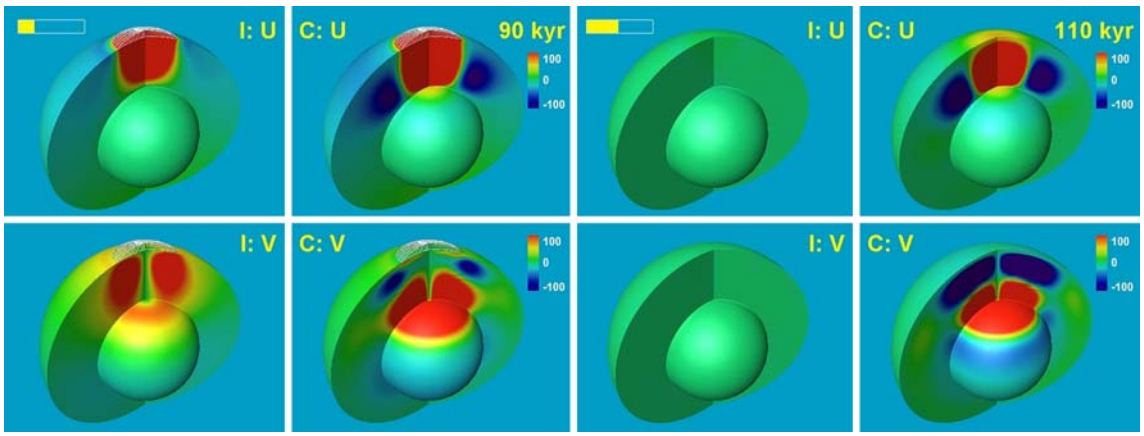

Fig. 6 Vertical and horizontal displacement (*top* and *bottom rows*, respectively) in a simple 3-layered model consisting of the core, the mantle and the lithosphere, each layer of constant density and elastic parameters. *Red color* means the depression in the vertical direction and points out off-the-axis movement in the horizontal direction. The mantle bulk modulus makes a substantial difference in the responses of incompressible (*left columns*) and compressible models (*right columns*). While at the loading maximum (*left 4 panels*) one can suspect the responses of the compressible model only because of the high amplitudes of the horizontal displacement in the deep mantle, after next 20 kyr the instability emerges in the whole mantle (*right 4 panels*) and then—with no surface loading at all—a quick gravitational collapse of the compressible model develops. The relaxation to zero amplitudes of vertical and horizontal displacement (panels labelled *U* and *V*, respectively) of the incompressible (*I*) model and the exponential collapse of its compressible (*C*) twin are unveiled in Movie 2 in the time interval lasting from 0 to 500 kyr. The animation speed is decreased during the loading episode

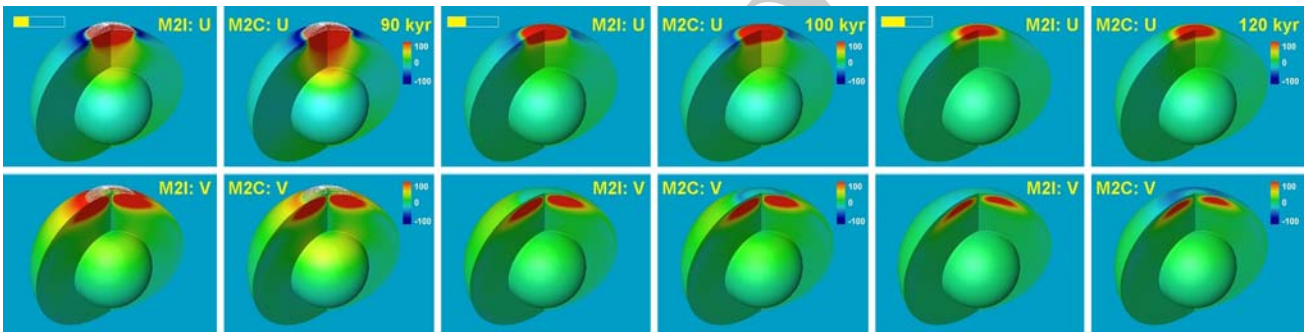

Fig. 7 Vertical and horizontal displacements in the incompressible (*left columns*) and compressible (*right columns*) PREM model with viscosity profile M2 at 90, 100 and 110 kyr. The compressible PREM model does not exhibit such a degree of gravitational instability, as in the 3-layered model in Fig. 6. The entire ice-age cycle for the two models is captured in Movie 3, where the labels are again *I* and *C* for incompressible and compressible models

of hundreds metres throughout the whole mantle up to CMB, while the magnitude is substantially less in the incompressible model. Similarly, we can recognize a significant difference in the horizontal displacements on the surface of the both models at 110 kyr. We show the viscoelastic responses for the PREM model and the viscosity profiles M1, M2, M3 and M4 in Fig. 8 and Movies 4 and 5.

Time-dependent dissipative heating (Hanyk et al. 2005) from the viscoelastic flow in the same set of models at 90 (top row), 100 (middle row) and 120 kyr (bottom row) is presented in Fig. 9. The values are normalized with respect to the chondritic radiogenic heating (3×10^{-9} W/m^3). The heating maxima, which we call the "heat flashes", emerge at 100 kyr, when the strain rate is highest. In Movies 6 and 7 (0–200 kyr) we see the development of the viscous heating (labelled D in the bottom panels) along with the horizontal displacement (top panels) for the non-LVZ and LVZ models, respectively.

Discussion and perspectives

Over the last few years, visualization has progressed from a tool employed by relatively few researchers to understand their data into a relatively easy-to-use tool and the importance of visualization in computational geophysics has been underscored in a recent report by Cohen (2005). In this technical paper, we have shown how to make use of the visualization package Amira (http://www.amiravis.com) together with Google Earth (http://www.earth.google.com)

Journal : 10069 Dispatch : 26-6-2007 Pages : 11
Article No. : 7 LE TYPESET
MS Code : 7 CP DISK

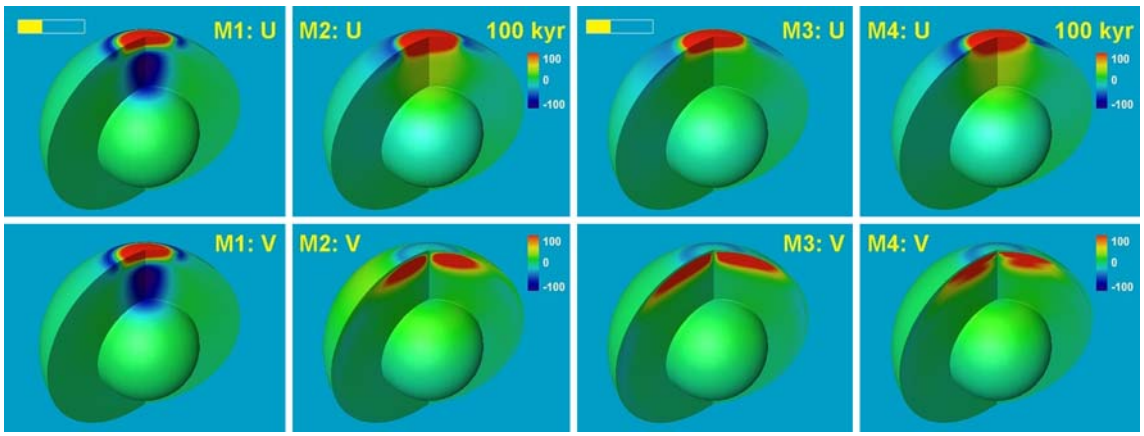

Fig. 8 Vertical and horizontal displacement (*top* and *bottom rows*) in the PREM model with viscosity profiles *M1*, *M2*, *M3* and *M4* (*columns* from *left* to *right*) when the ice sheet disappeared. It is obvious that the *M1* mantle is deformed substantially more than the high-viscous mantle of the other models. Similarly, the effect of the low-viscosity zone of the models *M3* and *M4* can be distinguished in farther-reaching increased horizontal deformation in the upper mantle. The action snapshotted for models *M1* and *M2* in the *left 4 panels* is animated in Movie 4 for the entire ice-age cycle followed by a free decay stage. Movie 5 shows the responses in the vertical and horizontal displacements to the ice-age cycle for the *M3* and *M4* models. The movies slow down temporarily within the period of the fast responses from 90 to 110 kyr of the ice-age cycle, i.e., during the phase of fast disintegration of the load and 10 following kyr

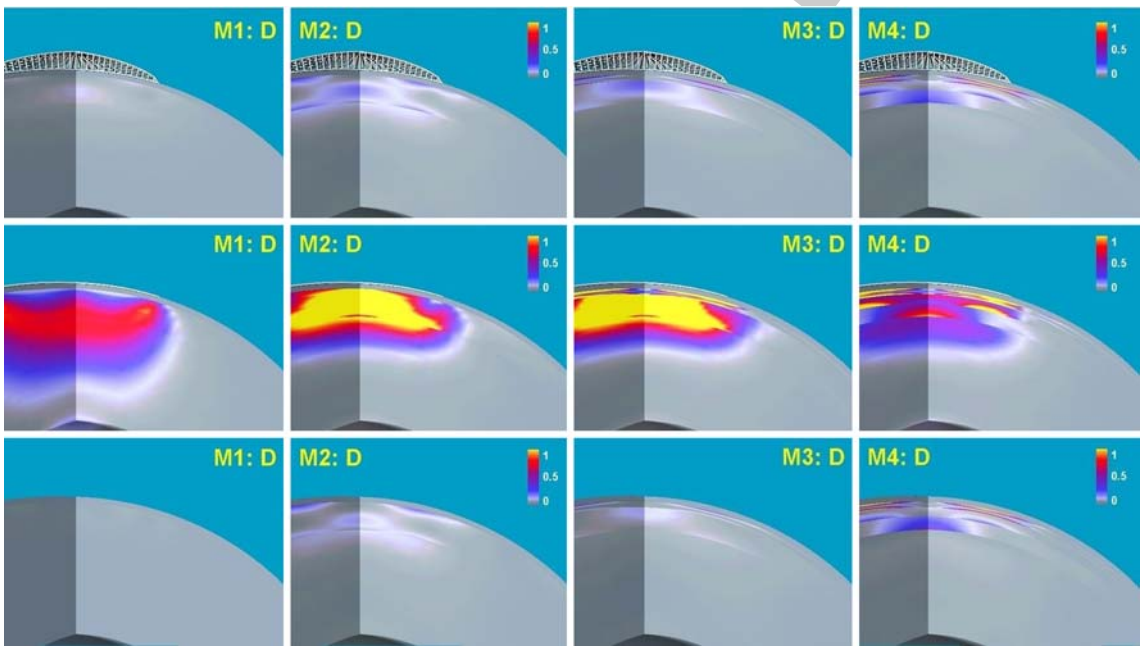

Fig. 9 Dissipative heating from the viscoelastic flow in the PREM model with viscosity profiles *M1*, *M2*, *M3* and *M4* (columns from *left* to *right*) at 90 (*top row*), 100 (*middle row*) and 120 kyr (*bottom row*). The values are normalized with respect to the chondritic radiogenic heating (3×10^{-9} W/m^3). The heating maximum appears at 100 kyr when the strain rate is the highest. Movies 6 and 7 (0–200 kyr) show the development of the "heat flashes" along with the horizontal displacement for the non-LVZ and LVZ models, respectively

to improve our understanding of the time-dependent dynamics associated with the postglacial isostatic readjustment. Visual techniques used in the past to enhance data understanding, beyond looking at rows of numbers on computer printouts, have been restricted to simple line plots and two-dimensional graphics and not much work has been carried out on time-dependent surface renderings of computational data sets of the order of $100 \times 100 \times 100$ spatial points and around 1,000 time steps. With the impending arrival of peta-scale computers, time-dependent simulations will become commonplace and movies will be in high demand.

We have demonstrated here the feasibility of using the Amira package for understanding better certain

Journal : 10069 | Dispatch : 26-6-2007 | Pages : 11
Article No. : 7 | ☐ LE | ☐ TYPESET
MS Code : 7 | ☑ CP | ☑ DISK

time-dependent features of postglacial rebound. These include (1) the differences in the physics of viscoelastic relaxation process between the compressible and incompressible elastic models, (2) the differences in the relaxation and transient flow dynamics of models with different mantle viscosity profiles, (3) the different forms of shear heating for diverse viscosity stratifications. We have also incorporated the Google Earth framework for enhancing our visualization and comprehension capabilities. This can be utilized further within the framework of a digital Earth setup.

Finally, many of these modules developed here can easily be transferred for visualizing tsunami waves propagating over ocean basins in spherical Earth model (cf. Liu et al. 2005; Yuan et al. 2006; Zhang et al. 2006), tidal deformation (Xing et al. 2007) and also InSAR images acquired by satellites (e.g., Furuya and Wahr 2005).

Acknowledgments We thank Ying-chun Liu, Huai Zhang, Ben Kadlec and Xiaoru Yuan for stimulating discussions and Lapo Boschi and Georg Kaufmann for valuable comments. This work has been supported by Research Program MSM0021620860 of the Czech Ministry of Education, NSF's ITR and CMG programs.

Appendix A. Overlays on a virtual globe by means of Google Earth

Since its inception in 2005, Google Earth has become a popular server-client based virtual globe program (http://www.earth.google.com). Users can directly view the geological features in three-dimensional perspective projections, instead of just over flat maps. With the recent advent of Google Earth, we feel it timely to integrate the postglacial rebound results with this innovation in software engineering, which has many implications for digital map technology and web applications. Postglacial isostasy takes place over specific geographical areas on the globe. Therefore, it is helpful for the reader to be provided with contextual geographical information. In this work we have integrated the visualization results into Google Earth by using the image overlay function provided by Google Earth, which turns out to be very useful.

First, we have prepared data files in the form of a time series of AmiraMesh files with rectilinear coordinates. Then, within Amira, we employed the HeightField module to create appropriate views, which we saved to 2D bitmap images using the Snapshot tool. Unfortunately, Amira does not have the capability to save images with selected colors marked as transparent and the images have to be recoded into the PNG or GIF format in a third-party software, such as ImageMagick (http://www.imagemagick.org), if color transparency is desired. In our case, we made the black-and-white images with the white reserved for the ice coverage and the black marked as transparent. The vector graphics, like PostScript output from Generic Mapping Tools (http://gmt.soest.hawaii.edu), cannot be imported into the bitmap-oriented framework of Google Earth and needs to be converted beforehand.

The first image of the series we then imported into Google Earth using its "Add Image Overlay" module, which allows to place the bitmap on the spherical rectangle of the globe determined by the geographical latitudes and longitudes (Fig. 10). Note that there is also available a tool for setting the transparency level of the whole image which may be used to get the topography covered by ice sheets partially visible. Then we set up the "Time-Based Refresh"

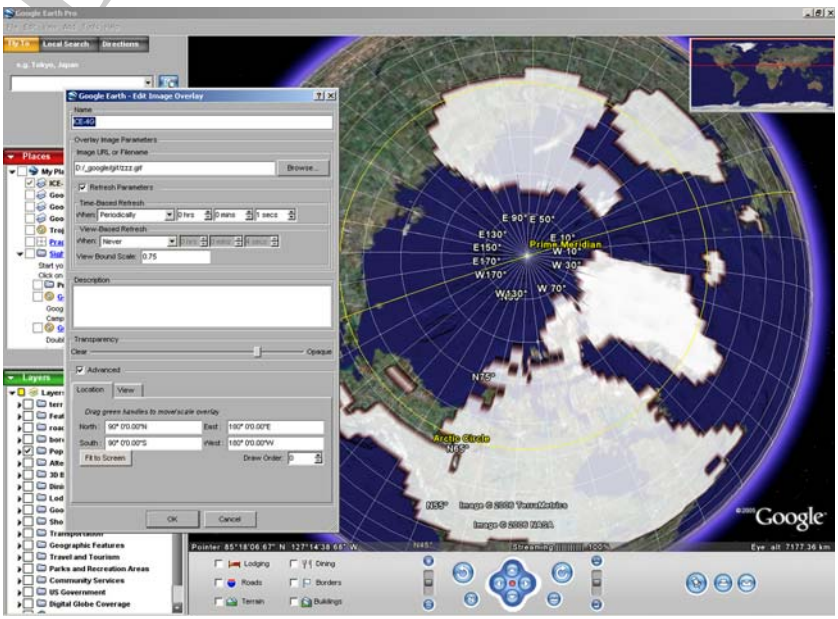

Fig. 10 Google Earth in action: a transparent GIF image with the ice coverage in the last glacial maximum (Peltier 1994) is overlaid on the present-day topography

Journal : 10069 | Dispatch : 26-6-2007 | Pages : 11
Article No. : 7 | ☐ LE | ☐ TYPESET
MS Code : 7 | ✔ CP | ✔ DISK

tool to force the automatic refresh of the overlaid image which we started to replace in parallel with the same frequency by means of a user script. The resulting movie-like effect can be recorded by the "Movie Maker" module or by taking snapshots of the images one by one and converting them into a movie by a third-party software (e.g., VirtualDub, http://www.virtualdub.org).

Movie 1 (http://geo.mff.cuni.cz/~lh/papers/07visgeo, http://www.msi.umn.edu/~ladah/07visgeo) depicts the evolution of the ice coverage in the last 21 kyr as described by the ICE-4G model (Peltier 1994). The maps of the ice coverage prepared by Amira with the transparency of the black color added by ImageMagick are overlaid on the northern hemisphere of Google Earth. The movie is made from 22 JPG files with the resolution 1,000 × 800 pixels and size 170 KB each, with the total movie size of 520 KB after the encoding in VirtualDub with the DivX compression.

A service similar to Google Earth becomes recently available at the Windows Live web page (http://www.local.live.com). The 3D engine, Microsoft Virtual Earth 3D, is in its Beta version at present and we must wait for its further development.

Appendix B. Visualization on a sphere using Amira

Amira is an advanced modern tool for 4D visualization in both the 3D space and time (http://www.amiravis.com). It is a commercial package available on many platforms, ranging from Linux and Microsoft Windows to Macintosh. The extensive set of easy-to-use features includes data imaging on the Cartesian, curvilinear and finite-element grids, scalar and vector field visualization algorithms, computation of iso-surfaces, direct volume rendering, time series manipulation, creating movies, support for the Tcl scripting language (http://www.tcl.tk), batch programming and remote data processing and remote visualization (see Erlebacher et al. 2006). There is an active research front backing up Amira's constant advancement in visualization. In contrast, Paraview (Parallel Visualization Application, http://www.paraview.org) is an open-source software, which has been applied, e. g., to 3D visualization of turbulence by Goldstein et al. (2005). Here we describe the steps made by us in visualizing with Amira the time evolution of a deformed Earth described by spherical coordinates, i.e., during preparation of Movies 2–7. The flowchart of the visualization process is given in Fig. 11, a screen dump of Amira running on the MacOs system in Fig. 12.

The first step is to prepare data files for Amira. These files, called AmiraMesh files, must contain properly formatted headers with details on enclosed physical 3D fields, including the grid size and (integer or real) data type. The spherical body, with which we deal, is best represented by a special kind of AmiraMesh format, which includes a section of all the grid coordinates. We have written a Fortran subroutine for data setup on a hollow shell, which consists of a spherical outer surface, an interior spherical surface (the core-mantle boundary) and up to three interior cuts through the mantle, as apparent from Fig. 13. These configurable hollow shells are advantageous for visualization of fields

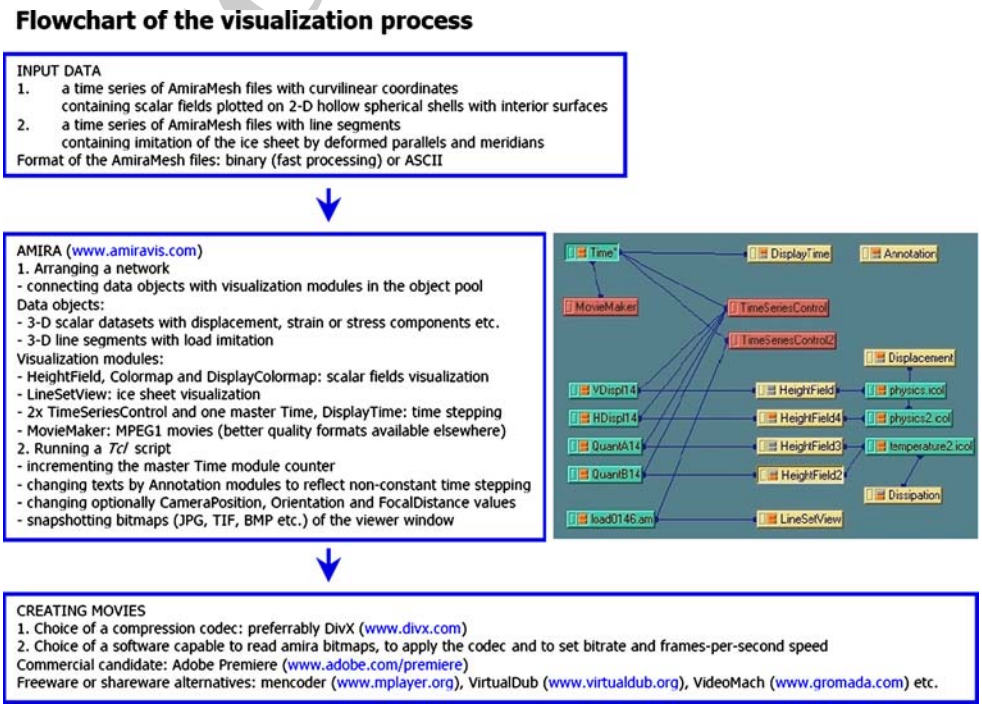

Fig. 11 Flowchart of the visualization process

Journal : 10069 Dispatch : 26-6-2007 Pages : 11
Article No. : 7 ☐ LE ☐ TYPESET
MS Code : 7 ☑ CP ☑ DISK

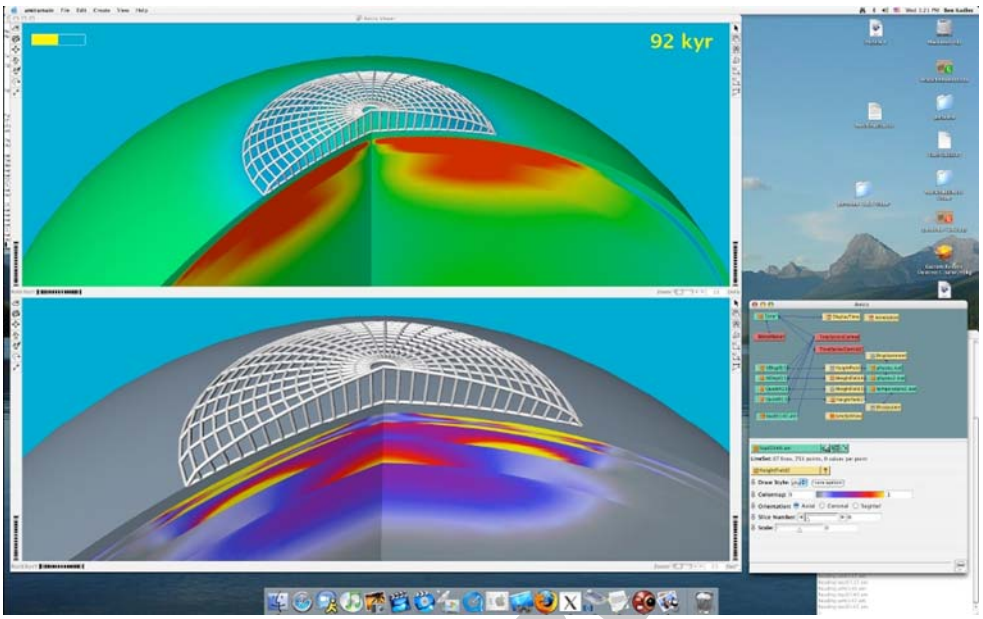

Fig. 12 Screen dump of Amira running on MacOS

with an axial symmetry and can also be used for attractive insights into 3D fields. The main benefit of employing the hollow shells is a low memory requirement, which allows us to visualize time processes with a long duration.

The next key step is the import of the time series of AmiraMesh files into Amira. We tested two techniques, each with its pros and cons. The more straightforward one is based on loading a large number of data files, each representing one time step. The Time module in Amira is automatically launched which allows easy handling data in time and attaching the MovieMaker module. However, the drawback emerges, when the number of data files is too large. The reading speed of a time series first drops, when a few hundred files are loaded, but this decrease can be avoided by turning off Amira's data cache. (Cached files can be accessed around five times faster then the original data files, as far as the amount of data does not reach the physical memory size or the number of files is a few hundred. The caching management then can result in access times for cached files substantially worse then for non-cached files.) The reading speed drops again when around 1,000 files are read, apparently because of Amira's implementation of internal file indexing, as it is independent on the total data size. Actually it prevents one from applying this method for visualizing such long time series.

The second technique makes use of the fact that our visualized data are only 2D shells. The unused capacity for the third spatial dimension can be used for the time instead. The whole time series can thus be saved in a single file, which can always be loaded fast. The animation of the coordinate planes along this "temporal dimension" can be performed by the Animate module and actually mimics the time evolution. There is no problem with the synchronization of more AmiraMesh files, because one Time module can master several Animate modules. Unfortunately, this technique is not applicable for all types of AmiraMesh files, namely for the line-segments format used for describing curves. This important file format does not provide a mean for selection of a particular piece of a curve, and curves evolving in time must be imported into Amira by the former technique. We employed the line segments to mimic the ice sheet in Fig. 4.

In both cases, the import speed of data files can be improved by a factor of 3, when the input files are binary. We point out that Amira internally stores all real data in double precision, no matter the precision of data in input files. This is a questionable feature: such a high accuracy might be redundant for visual output intended for a human

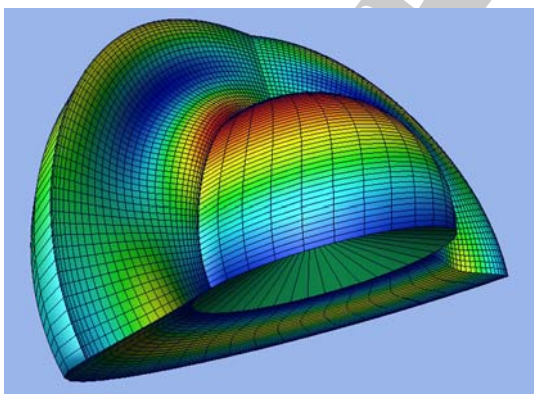

Fig. 13 A hollow shell with two spherical surfaces and three interior cuts. The low-memory requirement for this object allows to visualize long series of time-dependent data. Here, the shell is deformed in accordance with the horizontal displacement of the toroidal normal mode ${}_2T_2$

Journal : 10069 Dispatch : 26-6-2007 Pages : 11
Article No. : 7 LE TYPESET
MS Code : 7 CP DISK

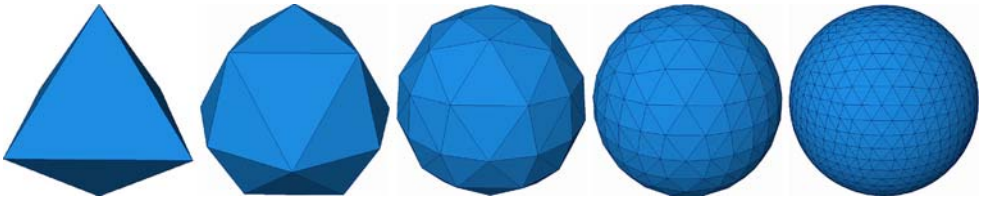

Fig. 14 Tetrahedral finite-element mesh approximation of a sphere in Amira

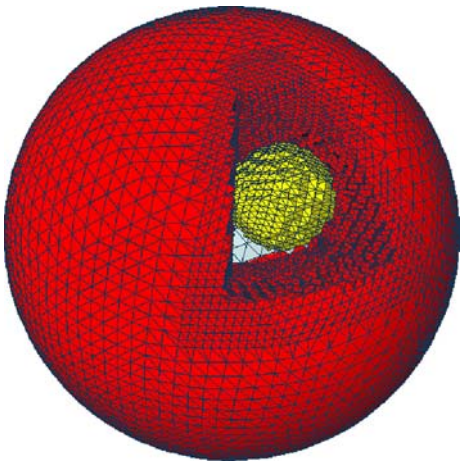

Fig. 15 A tetrahedral mesh of higher complexity with local refinement. The model of two nested spheres is used for benchmark purposes with analytical results

eye, and even restricting, when the total size of data reaches the amount of available memory.

For most of our movies we employed the HeightField, LineSetView and several auxiliary modules (DisplayTime, DisplayColorMap, Annotation), configurable straightforwardly. The movies made by the Movie Maker module can be saved in the MPEG or AVI formats with low compression only. It is therefore worthwhile to prepare a script for taking a control of the Time module and saving snapshots into bitmap images (JPG, lossless TIFF or EPS). The resulting series of images can be converted into a movie by a third-party software (e.g., VirtualDub, http://www.virtualdub.org).

Beside imaging the spherical shells described by curvilinear coordinates, we also tested the capability of Amira for visualizing objects defined on unstructured grids used in finite element modelling of postglacial rebound. We present increasingly accurate approximations of a sphere by tetrahedral elements in Fig. 14. The finite-element grid generator (Everett 1997) is based on recurrent subdivision of tetrahedra which is started from the initial octahedral approximation of a sphere. The grid is stored in terms of node coordinates and quadruplets of indices pointing at the four vertices of each tetrahedron. This structure can be easily implemented using the binary AmiraMesh format.

A sample of a locally refined tetrahedral mesh for the sake of two-nested-spheres benchmark with analytical results is shown in Fig. 15 (Velimsky et al. 2006).

Material parameters, such as viscosity, density, Lamé's elastic coefficients, and modelled variables, such as displacement, perturbed gravitational potential, and stress tensor components are assigned to nodes or tetrahedral, respectively, in piecewise-linear and piecewise-constant fashion and are stored in the same file. Moreover, we implemented local refinement and arbitrary positioning of radial interfaces. Visualization possibilities for tetrahedral grids in Amira comprise a wide spectrum of techniques including cross-sections, isolines, isosurfaces, streamlines, streamsurfaces and vector arrows.

References

Alley RB, Clark PU, Huybrechts P, Joughin I (2005) Ice-sheet and sea-level changes. Science 310:456–460

Cathles LM (1975) The viscosity of the Earth's mantle. Princeton, New Jersey

Cohen RE (2005) High-performance computing requirements for the computational solid Earth sciences. http://www.geo-prose.com/computational_SES.html

Dziewonski AM, Anderson DL (1981) Preliminary reference Earth model. Phys Earth Planet Inter 25:297–356

Erlebacher G, Yuen DA, Dubuffet F (2001) Current trends and demands in visualization in the geosciences. Electron Geosci 6:3 doi: 10.1007/s10069-001-1019-y

Erlebacher G, Yuen DA, Lu Z, Bollig EF, Pierce M, Pallickara S (2006) A grid framework for visualization services in the Earth sciences. Pure Appl Geophys 163:2467–2483

Everett ME (1997) A three-dimensional spherical mesh generator. Geophys J Int 130:193–200

Farrell WE (1972) Deformation of the earth by surface loads. Rev Geophys Space Phys 10:761–797

Fornberg B (1996) A practical guide to pseudospectral methods. Cambridge, New York

Furuya M, Wahr JM (2005) Water level changes at an ice-dammed lake in west Greenland inferred from InSAR data. Geophys Res Lett 32:L14501 doi: 10.1029/2005GL023458

Goldstein DE, Kadlec BJ, Yuen DA, Erlebacher G (2005) Visualizing 3D turbulence on temporally adaptive wavelet collocation grids. Eos Trans AGU 86(52), Fall Meet Suppl, Abstract IN43B-0333

Hanyk L (1999) Viscoelastic response of the earth: initial-value approach. PhD Thesis, Charles University, Prague http://www.geo.mff.cuni.cz/~lh/phd

Hanyk L, Moser J, Yuen DA, Matyska C (1995) Time-domain approach for the transient responses in stratified viscoelastic Earth models. Geophys Res Lett 22:1285–1288

Journal : 10069 | Dispatch : 26-6-2007 | Pages : 11
Article No. : 7 | ☐ LE | ☐ TYPESET
MS Code : 7 | ☑ CP | ☑ DISK

Hanyk L, Yuen DA, Matyska C (1996) Initial-value and modal approaches for transient viscoelastic responses with complex viscosity profiles. Geophys J Int 127:348–362

Hanyk L, Matyska C, Yuen DA (1998) Initial-value approach for viscoelastic responses of the earth's mantle. In: Wu P (ed) Dynamics of the ice age earth: a modern perspective. Trans Tech Publ, Switzerland, pp 135–154

Hanyk L, Matyska C, Yuen DA (1999) Secular gravitational instability of a compressible viscoelastic sphere. Geophys Res Lett 26:557–560

Hanyk L, Matyska C, Yuen DA (2000) The problem of viscoelastic relaxation of the Earth solved by a matrix eigenvalue approach based on discretization in grid space. Electron Geosci 5:4 doi: 10.1007/s10069-000-1008-6

Hanyk L, Matyska C, Yuen DA (2002) Determination of viscoelastic spectra by matrix eigenvalue analysis. In: Mitrovica JX, Vermeersen BLA (eds) Ice sheets, sea level and the dynamic Earth, Geodynamics Series 29, AGU, pp 257–273

Hanyk L, Matyska C, Yuen DA (2005) Short time-scale heating of the Earth's mantle by ice-sheet dynamics. Earth Planet Space 57:895–902

Hays JD, Imbrie J, Shackleton NJ (1976) Variations in the Earth's orbit: pacemaker of the ice ages. Science 194:1121–32

Hetland EA, Hager BH (2006) The effects of rheological layering on post-seismic deformation. Geophys J Int 166:277–292

Latychev K, Mitrovica JX, Tromp J, Tamisiea ME, Komatitsch D, Christara CC (2005) Glacial isostatic adjustment on 3-D Earth models: a finite-volume formulation. Geophys J Int 161:421–444

Liu YS, Zhang H, Yuen DA, Wang M (2005) High-performance computing and visualization of tsunamis and wind-driven waves. Eos Trans AGU 86(52), Fall Meet Suppl, Abstract S51D-1034

Martinec Z (1999) Spectral, initial value approach for viscoelastic relaxation of a spherical Earth with a three-dimensional viscosity—I. Theory. Geophys J Int 137:469–488

Martinec Z (2000) Spectral-finite element approach to three-dimensional viscoelastic relaxation in a spherical Earth. Geophys J Int 142:117–141

Mitrovica JX, Forte AM (2004) A new inference of mantle viscosity based upon joint inversion of convection and glacial isostatic adjustment data. Earth Planet Sci Lett 225:177–189

Mitrovica JX, Vermeersen BLA (2002) Glacial isostatic adjustment and the Earth system. In: Mitrovica JX, Vermeersen BLA (eds) Ice sheets, sea level and the dynamic earth. Geodynamics Series 29, AGU, pp 3–32

Peltier WR (1974) The impulse response of a Maxwell Earth. Rev Geophys Space Phys 12:649–669

Peltier WR (1994) Ice age paleotopography. Science 265:195–201

Peltier WR (2004) Global glacial isostasy and the surface of the ice-age Earth: The ICE-5G (VM2) model and GRACE. Ann Rev Earth Planet Sci 32:111–149

Plag H-P, Jüttner H-U (1995) Rayleigh-Taylor instabilities of a self-gravitating Earth. J Geodyn 20:267–288

Prockter LM, Nimmo F, Pappalardo RT (2005) A shear heating origin for ridges on Triton. Geophys Res Lett 32:L14202

Ranalli G (1995) Rheology of the Earth. Chapman & Hall, London

Sabadini R, Vermeersen B (2004) Global dynamics of the Earth: Applications of normal mode relaxation theory to solid-earth geophysics. Kluwer, Dordrecht

Schiesser WE (1994) Computational mathematics in engineering and applied science: ODEs, DAEs, and PDEs. CRC, Florida

Siegert MJ (2001) Ice sheets and late quaternary environmental change. Wiley, Chichester

Spada G, Ricard Y, Sabadini R (1992) Excitation of true polar wander by subduction. Nature 360:452–454

Tromp J, Mitrovica JX (2000) Surface loading of a viscoelastic Earth—III. Aspherical models. Geophys J Int 140:425–441

Velicogna I, Wahr J (2002) Post glacial rebound and earth's viscosity structure from GRACE. J Geophys Res 107:2376 doi: 10.1029/2001JB001735

Velimsky J, Inovecky L, Matyska C (2006) (In)Finite element approach to modelling of viscoelastic relaxation of the earth. EGU, 3rd General Assembly, Vienna

Wu P, Peltier WR (1982) Viscous gravitational relaxation. Geophys J R Astr Soc 70:435–485

Wu P, Ni Z, Kaufmann G (1998) Postglacial rebound with lateral heterogeneities: From 2D to 3D modelling. In: Wu P (eds) Dynamics of the ice age Earth: a modern perspective. Trans Tech Publ, Switzerland, pp 557–582

Xing HL, Zhang J, Yin C (2007) Finite element analysis of tidal deformation of the entire earth with non-continuum out layer. Geophys J Int (in press)

Yuan X, Liu Y-C, Yuen DA, Chen B, Pergler T, Shi Y (2006) An efficient method for creating InSAR-like images. Pure Appl Geophys (submitted)

Zhang H, Shi Y, Yuen DA, Liu YC, Zhang C, Yuan X (2006) Modelling and visualization of tsunamis. Pure Appl Geophys (submitted)

Journal : 10069 | Dispatch : 26-6-2007 | Pages : 11
Article No. : 7 | ☐ LE | ☐ TYPESET
MS Code : 7 | ☑ CP | ☑ DISK